Materials Today Physics 27 (2022) 100816

Contents lists available at ScienceDirect

Materials Today Physics

journal homepage: www.journals.elsevier.com/materials-today-physics

Distinct optical and acoustic phonon temperatures in nm-thick suspended WS_2: Direct differentiating via acoustic phonon thermal field invariant

S. Xu [a,1], N. Hunter [b,1], H. Zobeiri [b], H. Lin [c], W. Cheng [d,**], X. Wang [b,*]

[a] School of Mechanical and Automotive Engineering, Shanghai University of Engineering Science, Shanghai, 201620, PR China
[b] Department of Mechanical Engineering, 2025 Black Engineering Building, Iowa State University, Ames, IA, 50011, USA
[c] School of Environmental and Municipal Engineering, Qingdao University of Technology, Qingdao, Shandong, 266033, PR China
[d] Department of Thermal Science and Energy Engineering, University of Science and Technology of China, Hefei, Anhui, 230027, PR China

ARTICLE INFO

Keywords:
Optical and acoustic phonon temperature difference
Intrinsic thermal conductivity
Raman based thermal probing
Suspended 2D materials
Geometry-dependent thermal field invariant

ABSTRACT

Under highly focused photon irradiation, the cascading energy transport and resulting temperature difference between optical phonons (OPs) and acoustic phonons (APs) in 2D materials is one critical problem in Raman-based energy transport characterization. Despite reported theoretical and experimental work, this problem remains poorly solved and renders the measurement results invalid since Raman thermometry only measures OP temperature while heat conduction is sustained by APs. Here an AP thermal field invariant is constructed to rigorously distinguish OP and AP temperatures. The Raman-measured counterpart differs from this invariant and reflects the effect of OP-AP temperature difference. It is found that under 0.38 μm radius laser heating, the OP-AP temperature difference is 37.6% of AP temperature rise for a 22 nm suspended WS_2, confirming the strong OP-AP thermal non-equilibrium. For the first time, the real thermal conductivity of 2D WS_2 is measured based on AP temperature. Furthermore, the energy coupling factor between OPs and APs is determined to $\sim 10^{14}$ $Wm^{-3}K^{-1}$ under rigorous optical interference consideration. Our AP thermal invariant methodology can be generalized to Raman-based thermal conductivity measurement of suspended 2D materials of arbitrary geometry, and will enable high-level rational material design toward great performance.

1. Introduction

2D materials such as graphene, transition metal dichalcogenides (TMDs) [1], hexagonal boron nitride (h-BN) [2], graphyne [3], noble metal dichalcogenides (NMDs) [4], elemental 2D materials [5], 2D transition-metal carbides, carbonitrides, and nitrides(MXenes) [6] exhibit unusual physical properties due to the extreme reduction in one dimension down to the atomic level. Both the resulting large surface to volume ratio and strong confinement of electrons and carriers to sub-nanometer lengths contribute to the emergence of unique features in 2D materials that differ from their bulk counterparts. They fit well for multiple applications where their bulk counterparts do not. 2D TMDs [7] and black phosphorus [8] are good candidates for transistors because of their high charge mobility and moderate bandgaps. Also, they have high visible light absorption as monolayers and can be applied to high efficiency photodetectors in compact packaging [9–11]. Besides, single-layer MoS_2 and 2H–$MoTe_2$ were experimentally revealed to possess strong piezoeletronic effect. Coupled with its semiconducting properties, they could be applied to piezoelectronics [12,13]. $CaSi_2$ films with buckled silicone structure controlled by Ca intercalation exhibited a much larger Seebeck coefficient than the theoretical prediction, and would be comparable to the state-of-the-art thermoelectric materials [14]. 2D-connectivity ternary anisotropic compound $Ga_2I_2S_2$ showed high anisotropic TE conversion efficiency [15] at room temperature in theoretical investigation. Furthermore, due to their unique structural and electronic properties, 2D materials have also been extensively studied in catalyst field and exhibited high efficiency and stability [16,17]. Along with the wide application of micro/nano-devices involving 2D materials, thermal management requires close attention in order to guarantee successful device performance since their physical properties are very temperature sensitive. The thermal conductivity and interface thermal conductance are two key properties in thermal design. Due to

* Corresponding author.
** Corresponding author.
E-mail addresses: wlcheng@ustc.edu.cn (W. Cheng), xwang3@iastate.edu (X. Wang).
[1] Equal contribution authors.

https://doi.org/10.1016/j.mtphys.2022.100816
Received 7 August 2022; Accepted 9 August 2022
Available online 24 August 2022

the fact that 2D materials only have one or a few atomic layers in the thickness direction, they cannot be suitably measured using conventional thermal measurement methods. Instead, Raman thermometry is widely used for characterizing the thermal conductivity and interface thermal conductance of 2D materials [18–20].

Raman thermometry measures temperature based on the linear temperature response of a material's Raman spectrum. For a specific 2D material, the Raman shift and linewidth of characteristic peaks will change linearly with temperature within a moderate temperature range. Furthermore, in many cases the Raman excitation laser is used to do simultaneous heating and thermal probing. Balandin et al. [21] first used the steady state Raman method to measure the thermal conductivity of suspended graphene. This steady state Raman method has been widely adopted for thermal characterization 2D materials [22–25]. However, some critical issues arise in this steady state Raman technique [18]. Accurate optical absorption is required and is usually unknown for many new 2D materials. Besides, the temperature coefficient of Raman properties is needed as well. This critical parameter is calibrated in an additional experiment which causes unexpected local stress differentiation from the thermal characterization experiment.

Since then, great efforts have been paid to advance the steady state Raman technique. Xu et al. [26] developed a time-domain differential Raman (TD-Raman) method. In this method, the heating/excitation laser was specifically modulated such that in each cycle the heating time could be varied from very short (shorter than the thermal characteristic time) to very long (much longer than the thermal characteristic time). The thermal diffusivity of a silicon cantilever was determined from the changing rate of Raman peak properties against the laser excitation time. More importantly, the errors from unknown optical absorption measurement and Raman temperature coefficient calibration were avoided completely. Aiming at increasing the efficiency of TD-Raman, Wang et al. [27,28] developed a frequency-resolved Raman (FR-Raman) technique. They employed an amplitude-modulated laser instead and built a transient heat transfer model taking into account the heating effect from previous laser cycles. Limited by the ability of modulator, investigation of physical processes shorter than nanoseconds is harder to achieve using this method.

The FR-Raman technique greatly shortens the experimental time and provides a base for the development of diverse transient Raman methods. Yuan et al. [29,30] developed an energy transport state-resolved Raman (ET-Raman) using both continuous-wave (CW) and picosecond (ps) lasers. In a supported 2D MoS_2 layer, they realized a ps heat transfer scenario totally distinct from the steady state under CW laser heating. During such ultrafast ps duration, the generated heat primarily accumulates in the MoS_2 layer rather than being conducted away through the interface by hot carriers and phonons. For the first time, they measured both the interface thermal resistance and hot carrier diffusion coefficient in a supported 2D semiconductor using the ET-Raman method. Later, Hunter et al. [31] pointed out that radiative electron-hole recombination following photon energy absorption in monolayer 2D materials must be considered to fully evaluate interface energy transport. They introduced a nanosecond (ns) laser to build a new energy transport state between those under ps laser heating and CW laser heating and characterized the conjugated hot carrier and phonon transport while also measuring the electron-hole radiative recombination efficiency. However, the pulse energy of the ps or ns laser in ET-Raman is so high that could easily burn samples, especially suspended 2D materials. Also, different types of laser sources could raise different thermal nonquilibrium in one sample and thus significantly affect the accuracy of the measured thermal properties. To solve these problems, the frequency-domain energy transport state-resolved Raman (FET-Raman) technique [32,33] was then developed. By utilizing amplitude-modulated CW laser instead of ps and ns laser, FET can effectively eliminate the damage and different thermal nonquilibrium-induced uncertainties while maintain the ability of generating various transient energy transport states as those in ET-Raman.

The sensitivity and measurement uncertainty of the above methods greatly depends on the physical mechanisms and experimental operation. From the prospective of physical mechanisms, TD-Raman has the best sensitivity as its probing pulse is independent of each other, but the Raman signal collected in the short pulse duration (~several microseconds) has a low signal to noise ratio, which will lower the sensitivity of the method. In FR-Raman, the laser-off duration is short so that the Raman signal from the current pulse duration will be affected by the temperature evolution from previous pulses. This will lower the measurement sensitivity. ET-Raman employs ps or ns laser together with a CW laser. The difference in the laser source will cause measurement uncertainties due to different thermal nonequilibrium states under laser irradiation. Furthermore, the high laser intensity in the ultrafast pulse duration will easily burn samples, especially suspended 2D films. The comparison in measurement ability, advantages, drawbacks, and sensitivity of these Raman techniques is listed in Table 1. More details about the comparison of these methods can be found in Refs. [18,20,34].

In most Raman-based experimental work, no matter the steady state or transient Raman methods, a focused laser beam is usually used to achieve extremely localized heating. As a result, strong phonon mode-wide nonequilibrium exists. Vallabhaneni [35] and Lu [36] et al. found out that the energy transfer from incident photons to acoustic phonons under laser irradiation involves multiple energy carriers, including photons, electrons, optical phonons (OPs) and acoustic phonons (APs). Among them, APs are the major carriers transferring heat over a long-range distance. They questioned the accuracy of Raman thermometry which only measures OP temperatures. Sullivan et al. [37] applied a first principles multi-temperature model to calculate the local temperatures of electrons and phonons and demonstrated that the temperatures of these energy carriers are in a state of strong nonequilibrium. Lu et al. [36] showed that the most significant nonequilibrium is between cross-plane acoustic (ZA) phonons and other branches of phonons. Since ZA phonons are the main energy carriers in heat conduction, neglecting the nonequilibrium between acoustic and optical phonons will significantly underestimate the thermal conductivity of a material derived from Raman measurements.

In our recently published work, Wang et al. [38] investigated the energy transport from photons to optical phonons and proposed that the optical-acoustic phonon temperature difference only depends on the diameter of the incident laser spot when the total laser energy fluence is fixed. For the first time, they distinguished optical and acoustic phonon temperatures by evaluating the trend of measured temperature rise against laser spot size. However, the measurement was based on several assumptions and approximations that need significant improvement and revisit. First, the laser spot size in the measurement was limited by the physical experimental setup. Therefore the extrapolation method and the determined in-plane thermal conductivity suffered large uncertainties. Second, the theoretical calculation of acoustic phonon temperature under irradiation needed the thermal conductivity of the 2D material. They measured it under the assumption that the optical and acoustic phonon temperature difference could be neglected using a large heating spot. Such treatment sometimes has very large uncertainties, especially for high thermal conductivity materials. Third, the generated thermal nonequilibrium states under CW laser and nanosecond laser irradiation are very different due to the different hot carrier densities. This will lead to different optical-acoustic phonon thermal nonequilibrium. Finally, incomplete evaluation of the local incident laser intensity in the 2D material layer in that work led to additional measurement errors in the resulting thermal conductivity. These hinder higher-level understanding of the thermal nonequilibrium between optical and acoustic phonons. Subsequently, Zobeiri et al. [33,39] reported related work investigating the optical-acoustic phonon thermal nonequilibrium in graphene paper and supported multi-layer 2D materials. Though they further evaluated the interference effect-induced enhancement in the local laser intensity, the approximation in the physical model would lead

Table 1
Comparison in property measurement, advantages, drawbacks and sensitivity of four Raman techniques.

Methods	Reported property measurement	Advantages	Drawbacks	Sensitivity
TD-Raman	Thermal diffusivity/ conductivity	Simple physical model	Time consuming for short laser-on measurement	Very sensitive
FR-Raman	Thermal diffusivity/ conductivity	Simple physical model; Moderate time cost	Extensive post-processing; Frequency limitation due to modulator	Less sensitive than TD-Raman
ET-Raman	Thermal conductivity; Interfacial thermal resistance; Hot carrier diffusivity	Fast measurement; Multiple energy transport state probing in spatial and time domains	Complex physical model; Extensive post-processing; Complex optical alignment; Sample damage	Very sensitive
FET-Raman	Thermal conductivity; Interfacial thermal resistance	Fast measurement; Moderate physical complexity; Moderate post-processing	Frequency limitation due to modulator	Less sensitive than TD-Raman, and comparable to FR-Raman

to some uncertainties. The energy transport and optical-acoustic phonon thermal nonequilibrium in supported 2D materials, nevertheless, are totally different from that in suspended ones. All these works point out significant optical-acoustic phonon temperature differences. Neglect of such nonequilibrium will lead to huge errors in thermal conductivity and interface thermal conductance measurements. The rather indirect methods developed in these works make the optical-acoustic phonon temperature determination suffer from large uncertainties.

So far, the effect of this nonequilibrium between optical and acoustic phonons on thermal conductivity measurements has yet to be rigorously characterized due to the inevitable large uncertainty in the existing physical models for suspended 2D materials. In this work, to rigorously measure the intrinsic thermal conductivity of suspended 2D materials, we first establish a physical parameter solely related to acoustic phonon temperature rises. This factor can be precisely determined based on laser heating conditions without knowledge of sample's thermophysical properties, so the uncertainty due to the abovementioned first and second issues can be eliminated in our new physical model. Experimental deviation from this value is used to identify the effect of optical-acoustic phonon temperature differences. FET-Raman is employed to build two different energy transport states with the totally same nonequilibrium state under different irradiation, so that uncertainties raised by the different thermal nonequilibrium (issue 3 above) could be completely removed from the physical and experimental prospective. After taking out the effect of optical-acoustic phonon temperature difference, the intrinsic thermal conductivity is measured with high accuracy. The spatial distribution of incident optical field and optical interference in the suspended film are fully considered to determine the energy coupling factor between optical and acoustic phonon branches to diminish uncertainties (issue 4) in measured coupling factors from our last work.

2. Optical and acoustic phonon thermal nonequilibrium

Our measurement of the OP-AP temperature difference is conducted in a rigorously designed physical frame. First, to strictly control and explicitly define the heat transfer process, a structure of suspended film over a hole in a highly thermally conductive substrate is employed in this work. Holes of two distinct diameters are fabricated in a single crystalline Si wafer using the focused ion beam (FIB) technique. Then, nanometer-thin WS_2 films are mechanically exfoliated from the bulk and transferred to the substrates carefully to completely cover the hole as shown in Fig. 1. More details of the sample preparation can be found in our previous works [32,40]. Two suspended WS_2 samples are prepared over two holes of different diameters. The diameter of the hole is 12.5 μm (sample #1) in Figs. 1a and 6.14 μm (sample #2) in Fig. 1c.

In Fig. 1a, the WS_2 film has already been placed over the hole judged by the continuous color around the hole in the optical image. Due to the color difference induced by the interference effect, the light circular area is the hole where this portion of WS_2 film is suspended. In the remaining area, the WS_2 film is supported by the Si substrate showing a light blue color. Also, good contact between the film and the substrate adjacent to the hole could be confirmed from the uniform color. In Fig. 1d and e, atomic force microscopy (AFM) characterization shows surface morphology details of the two samples. The roughness and thickness measurements are shown in Fig. 1f and g for sample #1 and in Fig. 1h and i for sample #2. The WS_2 film of sample #1 is 22 nm thick with a roughness of less than 0.5 nm, and for sample #2 the thickness is 26 nm and the roughness is less than 1 nm.

The green spots in Fig. 1a and c indicate the laser irradiation spot on the suspended sample. It is carefully positioned in the middle of the suspended area to induce sensible heat transfer in the sample film. However, as a two-dimensional semiconductor, WS_2 has an indirect bandgap (1.79 eV) [41] smaller than the energy of the incident photons (532 nm, 2.33 eV). Therefore, complex physics will happen under photon heating: most incident photon energy will excite electrons from the valence band to conduction band, and generate holes. Since the hot electrons have a short lifetime, they diffuse over a short distance, recombine immediately with holes, and release energy to local OPs. Given that OPs have a very low group velocity and low heat capacity, they do very little heat conduction in space. Instead, they will transfer thermal energy to APs that have a faster group velocity, higher heat capacity, and thermal conductivity. This will lead to strong thermal nonequilibrium between OPs and APs. In this work, we do not distinguish the temperature difference between AP branches. The term "AP temperature" refers to the average temperature of APs, also called "lattice temperature". Finally, the APs raise a moderate temperature rise in the sample film and transfer thermal energy to the heat sink/substrate. As shown in Fig. 1b, under the laser intensity profile, electrons receive the most energy from photons and have the highest temperature compared to phonons. The hypothetical temperature of OPs is higher than that of APs. This phenomenon will quickly diminish when approaching the edge of the irradiation spot and disappear outside the spot.

Heat conduction in the suspended WS_2 film with a centrally located heating spot can be well described by a two-dimensional heat conduction model in cylindrical coordinates. The heat convection and radiation at the sample surface is ignored because the surface area is so small (~several microns in radius) that both of them are insignificant compared to the heat conduction process in the film. Taking sample #1 as an example, the thermal resistance for both heat convection and radiation is about two orders higher than the in-plane heat conduction resistance, which forces 99% of absorbed photon energy to transfer in the film plane. Also, under continuous photon heating, the cross-plane heat conduction reaches the thermally steady state much faster than in the in-plane direction due to the nm-thin thickness of the film. The heat conduction along the radial direction dominates the overall thermal transport process and the model is reasonably simplified as one-dimensional. First of all, we explain the AP thermal field invariant using a simplified thermal resistance model. Rigorous consideration is

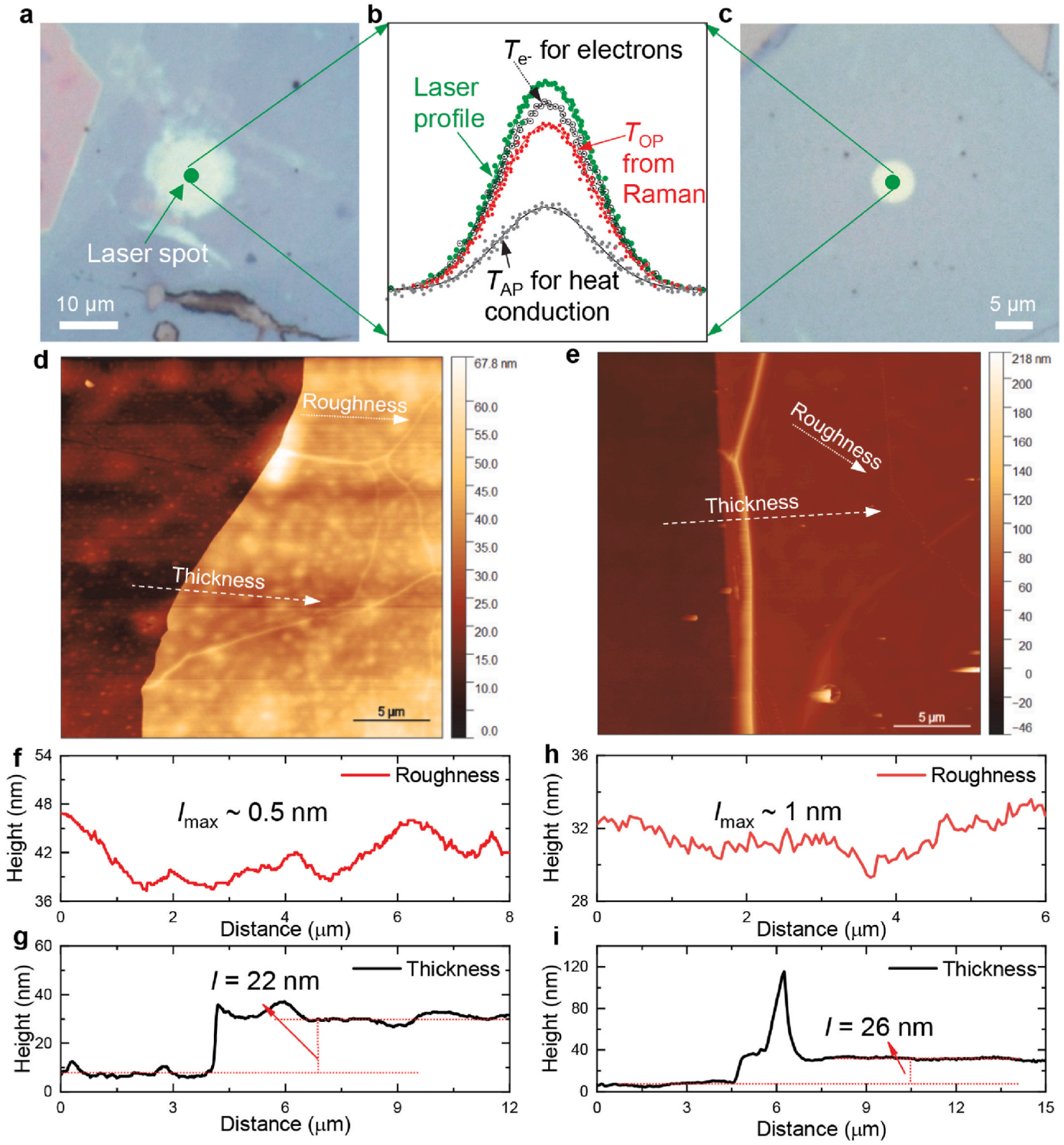

Fig. 1. Characterization of the two suspended WS_2 samples in the experiment. (a) Optical images of sample #1 suspended on a hole with a diameter of 12.5 μm. (b) Schematics of the hypothetical temperature rise of electrons (ɵ), OPs (red dots) and APs (black dots) under laser irradiation (green dots). (These dots are not experimental results). Under laser irradiation, energy transfers sequentially from photons to electrons, OPs, and then APs. (c) Optical image of sample #2 on a hole of 6.14 μm diameter. (d), (e) AFM images of sample #1 (d) and sample #2 (e) and the positions where the sample roughness and thickness are measured. (f), (g) Cross-sectional profiles of sample #1 show its roughness of 0.5 nm (f) and thickness of 22 nm (g). (h), (i) Cross-sectional profiles of sample #2 show its roughness of 1 nm (h) and thickness of 26 nm (i).

included in the numerical modeling.

Since the laser spot is very small (~μm), the temperature rise within it has a weak distribution and takes a value ΔT_{AP} here for ease of discussion. Its distribution is rigorously considered in our numerical modeling. The thermal resistance from the laser spot edge to the sample's edge is $R = \Delta T_{AP}/q = \ln(r_h/r_i)/(2\pi L\kappa)$, where q is the absorbed photon energy, L the film thickness, κ the intrinsic in-plane thermal conductivity, and r_h and r_i are the radii of the hole and laser spot, respectively. The subscript 'AP' denotes the AP temperature rise rather than that of OPs measured by Raman thermometry.

For one sample of r_h and κ, while r_i is a variable depending on the focusing system, we can create a new parameter termed AP temperature rise ratio ξ_{AP} with two different focusing scenarios employed,

$$\xi_{AP} = \frac{\Delta T_{AP,1}}{\Delta T_{AP,2}} = \frac{\ln(r_h) - \ln(r_{i1})}{\ln(r_h) - \ln(r_{i2})} \quad (1)$$

This new parameter is a ratio of the average temperature rise in the laser heated region. This ratio does not have the effect of thermal conductivity and is invariant regardless of the sample's κ. To verify this theoretical analysis, a corresponding simulation model is designed below to confirm the invariant ξ_{AP}'s negligible variation against κ. The governing equation of heat conduction for the suspended film is

$$\kappa \nabla^2 T_{cw} + \dot{q} = 0 \quad (2)$$

where T_{cw} is the steady-state temperature field in the film and $\dot{q}$ is the volumetric heating power, $\dot{q}(r,z) = I_0/\tau_i \exp(-r^2/r_0^2)[1 - \exp(-z/\tau_i)]$. τ_i is the laser absorption depth in the film defined as $\tau_i = \lambda/(4\pi k_i)$ in which λ is the wavelength of the incident laser and k_i is the extinction coefficient of the WS_2 film. With an incident laser of 532 nm, τ_i (WS_2) is 46.1 nm [42]. To match the real 2D energy transport situation during simultaneous Raman measurement and laser heating, the Gaussian

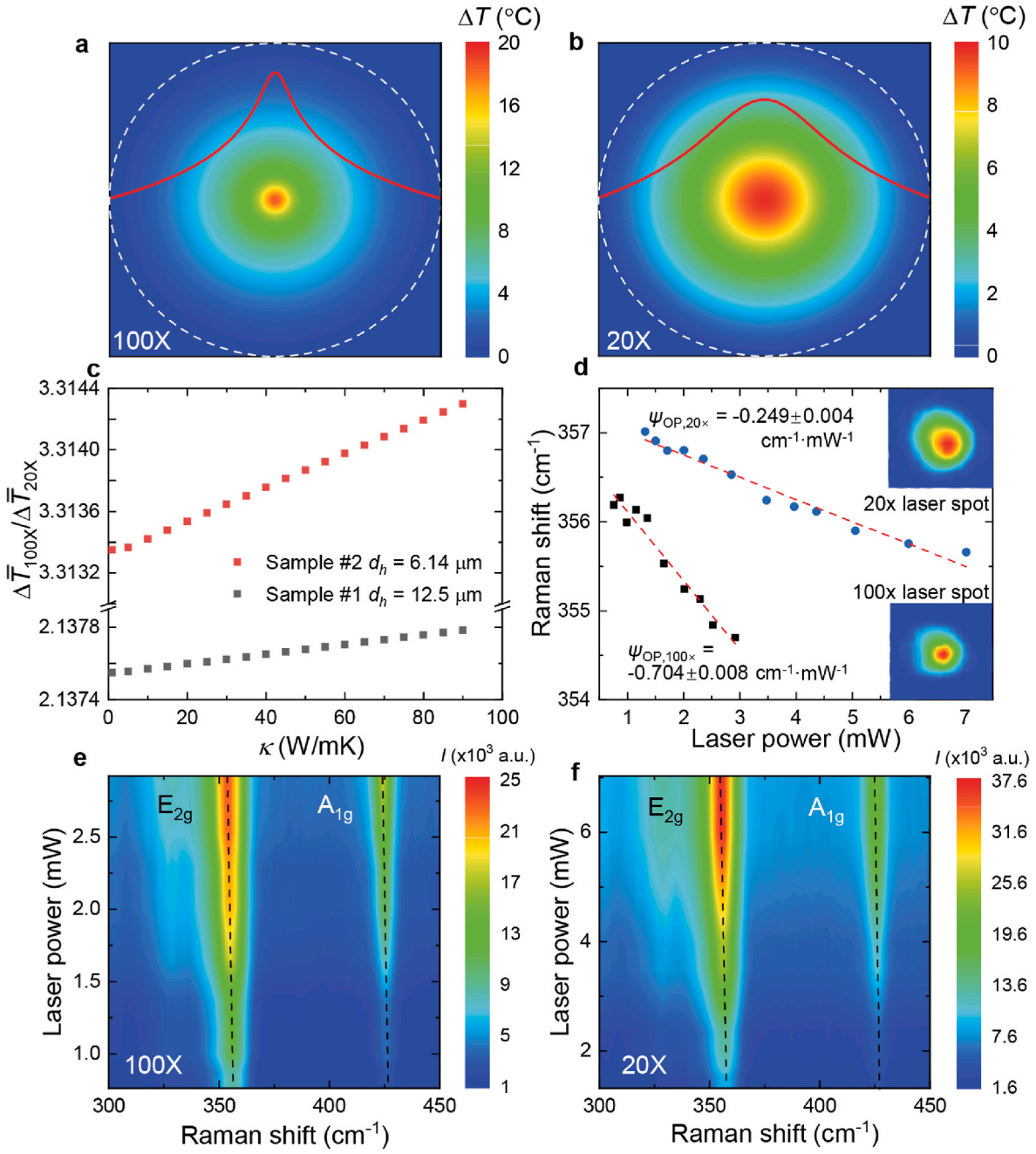

Fig. 2. Comparison between AP thermal field invariant with measured OP temperature rise ratio. (a), (b) High-fidelity computer modeling of AP temperature rise distributions over sample #1 under the 100 × objective (a) and 20 × objective (b). The red curve depicts the temperature variation from the center of the hole to the edge. The hole size of 12.5 μm is denoted by the white dashed line. (c) Simulated $\xi_{AP} = T_{AP,100\times}/T_{AP,20\times}$ variation against the intrinsic thermal conductivity for sample #1 suspended over a 12.5 μm hole and #2 suspended over a 6.14 μm hole. (d) Raman shift power coefficient ψ determination from the slope of Raman shift against the incident power for sample #1 under 20 × objective and 100 × objective. (e), (f) The contour of Raman intensity for sample #1 against the incident laser power under 100 × objective (e) and 20 × objective (f).

distribution of the incident laser as well as the Raman scatterings are considered. Thus, the determined temperature rise based on the collected Raman signal is naturally a Raman intensity-weighted temperature rise over the heating region, which has an expression as

$$\Delta\overline{T}_{cw} = \int_0^{V_0} I_R \exp(-z/\tau_i)\Delta T_{cw} dV \Big/ \int_0^{V_0} I_R \exp(-z/\tau_i) dV \quad (3)$$

where V_0 is the Raman scattering volume of the WS_2 film and I_R is the laser intensity within the film as $I_R = I_0 \exp(-r^2/r_0^2)\exp(-z/\tau_i)$. The term $\exp(-z/r_i)$ in Equation (3) reflects the Raman intensity attenuation when it leaves the scattering point to reach the top surface of the sample. Note here the complicated optical interference in the film is neglected. Such treatment will not affect our invariant calculation since the sample has negligible temperature distribution over its thickness direction. Using the structural parameters of sample #1 in modeling, the temperature fields at the thermally steady state under continuous laser heating are shown in Fig. 2. In our experiment detailed in the later section, both 20 × and 100 × objectives are selected for their distinct focusing spot sizes. Assuming 1 mW laser power absorption and a spot radius of 0.38 μm (at e^{-1}) under the 100 × objective, the maximum temperature rise reaches about 16.2 °C as shown in Fig. 2a. Under the 20 × objective, the laser heating spot radius is 1.68 μm (at e^{-1}) and the maximum temperature rise is around 9.5 °C (Fig. 2b). It is seen that within the laser heating spot, the temperature rise is very uniform. The temperature rise variation is 1.4 and 2 °C for the case of $r_i = 0.38$ μm and 1.68 μm, respectively.

The temperature rise ratio is calculated as $\xi_{AP} = \Delta\overline{T}_{AP,100\times}/\Delta\overline{T}_{AP,20\times}$ and the modeling results for sample #1 and #2 are shown in Fig. 2c. It is observed that for the 6.14 μm diameter hole, ξ_{AP} changes from 3.3134 to 3.3144 when κ increases from 1 to 90 $Wm^{-1}K^{-1}$. For such κ change, ξ_{AP} changes from 2.1376 to 2.1378 for the 12.5 μm hole case. These observations firmly confirm that ξ_{AP} is invariant with negligible effects from κ. Using Equation (1), our estimation gives ξ_{AP} of 3.465 and 2.131 for the 6.14 μm and 12.5 μm hole cases, very close to the precise modeling results shown in Fig. 2c. The tiny difference is due to the fact that the laser beam has a Gaussian distribution, not a spot with a clear cutoff at r_i. In Raman experiment, the measured ξ however is based on OP temperature rise as $\xi_{OP} = \Delta\overline{T}_{OP,100\times}/\Delta\overline{T}_{OP,20\times}$, and it carries the OP-AP temperature difference ΔT_{OA}. Wang et al. demonstrated that ΔT_{OA} is proportional to the local laser intensity [38]. Under constant laser energy irradiation, ΔT_{OA} is proportional to r_i^{-2}. Due to the effect of ΔT_{OA}, the Raman measured ξ_{OP} will differ from ξ_{AP}, and such difference can be used to determine ΔT_{OA} with high accuracy.

In Raman thermometry, the Raman wavenumber (Stokes scattering) will red shift with temperature rise [18]. However, the exact temperature response evaluation needs calibration of the Raman waver number temperature coefficient. This introduces additional errors to final measurement results [24,25]. A parameter termed Raman shift power coefficient, ψ, is proposed to eliminate these experimental errors [30]. It is defined as the Raman wavenumber shift per unit power, $\psi = \partial\omega/\partial P$. Thus, the correlation between temperature rise ΔT and ψ is $\psi = \chi_T \Delta T/(aP)$, where χ_T is the Raman shift temperature coefficient ($\chi_T = \partial\omega/\partial T$), a is the laser power absorption coefficient, and P is the incident laser power.

In the experiment, to realize fast and accurate determination of ψ, a lab-developed Raman system is improved by integrating a laser source and an automatic optical attenuation system in a commercial confocal Raman setup. The laser first enters the automatic optical attenuation system for power adjustment. The computer-controlled automatic optical attenuation system is able to adjust the laser energy by rotating a motorized neutral density filter and achieve different laser power levels with a minimum influence on the optical path. After that, the laser is directed into the confocal Raman as the excitation/heating source for thermal measurement. The illuminating system of the microscope is confocal with the excitation laser, making the laser spot/heating spot focused in the middle of the suspended area. Details of the Raman setup can be found in our previous work [32]. Raman results for sample #1 are shown in Fig. 2d–f. It is seen that both E_{2g} and A_{1g} peaks show visible (although small) redshifts in wavenumber when the laser power is increased. Since the A_{1g} peak is relatively weak and carries more uncertainty, the E_{2g} peak is used in our data analysis to evaluate the temperature rise. ψ is determined by linear fitting the wavenumber variation against the incident laser power (Fig. 2d).

An OP temperature rise ratio ξ_{OP} is introduced here as

$$\xi_{OP} = \frac{\Delta\overline{T}_{OP,100\times}}{\Delta\overline{T}_{OP,20\times}} = \frac{\chi_T\cdot(\partial\omega/\partial P)_{100\times}}{\chi_T\cdot(\partial\omega/\partial P)_{20\times}} = \frac{(\partial\omega/\partial P)_{100\times}}{(\partial\omega/\partial P)_{20\times}} = \frac{\psi_{100\times}}{\psi_{20\times}} \quad (4)$$

Thermal nonequilibrium between OPs and APs under continuous wave (CW) photon heating raises the temperature difference ΔT_{OA} between them as well as the difference between ξ_{OP} and ξ_{AP}. Since OPs have a negligible thermal conductivity compared with APs, almost all the energy that OPs receive from electrons will be transferred to APs. Theoretically, we have $\Delta T_{OA} \propto I/G$ where I is the local laser intensity and G is the OP-AP energy coupling factor. Notably, G is a constant in one sample no matter how large the heating spot is [38]. ΔT_{OA} is then averaged over the heating region and has a relation as $\Delta\overline{T}_{OA} \propto E_{tot}/r_i^2$ and E_{tot} is the total incident power over the laser spot. Under unit incident laser power, we can establish the relation between $\Delta\overline{T}_{OP}$ and r_i^2 as

$$\Delta\overline{T}_{OP} = \Delta\overline{T}_{AP,ri} + \Delta\overline{T}_{OA,ri} = \Delta\overline{T}_{AP} + C_{OA}/r_i^2 \quad (5)$$

where C_{OA} is a coefficient in the calculation process. Since $\xi_{AP} = \Delta\overline{T}_{AP,100\times}/\Delta\overline{T}_{AP,20\times}$ is already precisely determined based on the laser heating spot size and sample size, from the measured ξ_{OP} and Equation (5), we can finally obtain the percentage of $\Delta\overline{T}_{OA}$ over $\Delta\overline{T}_{AP}$ and also the contribution of $\Delta\overline{T}_{OA}$ to ψ.

In the Raman measurement, the 20 × and 100 × objective cases are used to determine C_{OA} because these two cases have the largest difference in r_i and will result in the highest accuracy in C_{OA} determination. For sample #1, $\psi_{20\times}$ is measured as -0.249 ± 0.004 cm^{-1} mW^{-1} and $\psi_{100\times}$ is -0.704 ± 0.008 cm^{-1} mW^{-1}. The higher value of $|\psi|$ indicates higher temperature rise under 1 mW laser irradiation, thus sample #1 has a higher temperature rise under the 100 × objective than the 20 × objective. According to the expression of the heat conduction resistance in the film plane, $R = \Delta T_{AP}/q = \ln(r_h/r_i)/(2\pi L\kappa)$, $R_{100\times}$ is larger than $R_{20\times}$ due to its smaller laser spot. This leads to a higher temperature rise and subsequent higher $|\psi|$ under the 100 × objective. $\psi_{100\times}/\psi_{20\times}$ is 2.83 $\pm$ 0.06, higher than the theoretical ξ_{AP} (= 2.137 in Fig. 2c), implying the existence of ΔT_{OA}. η ($= \Delta\overline{T}_{OA}/\Delta\overline{T}_{AP}$) is determined to be 4.1% and 37.6% for the 20 × and 100 × objectives. The results show that $\Delta\overline{T}_{OA}$ becomes significant under a more focused heating spot. The 50 × objective (r_i = 0.58 μm at e^{-1}) case is also investigated. $\psi_{50\times}$ is measured to be -0.555 $\pm$ 0.008 cm^{-1} mW^{-1} and $\eta_{50\times}$ is around 31.1%. The result using 20 × and 50 × objectives may have larger uncertainties because the difference between $r_{i,20\times}$ and $r_{i,50\times}$ is smaller than that between 20 × and 100 × objective cases. For this reason, for sample #2, only the 20 × and 100 × objective cases are considered. The measured ψ is -0.101 ± 0.002 cm^{-1} mW^{-1} and -0.394 $\pm$ 0.005 cm^{-1} mW^{-1} and η is 3.5% and 22.5% for the 20 × and 100 × objectives, respectively. All the calculated results are summarized in Table 2. For the 50 × objective case of sample #2, a large uncertainty in the determined ψ is caused by the visual difficulty in aiming the heating spot to the middle of the suspended sample area in the experiment. Thus, no result for the 50 × objective case of sample #2 is listed in Table 2.

Compared with sample #1, the ratio η of sample #2 is a little lower due to its higher level excited hot carrier concentration and resulting stronger OP-AP energy coupling (detailed in next section). For an even

Table 2
Summary of the size, ratio of $\Delta\overline{T}_{OA}$ to $\Delta\overline{T}_{AP}$, Raman measured ψ_{OP}, thermal conductivity, and energy coupling factor.

Sample	L/d_h	Objective/r_i [at e^{-1}]	η	ψ_{OP}[cm^{-1} mW^{-1}]	κ [W m^{-1} K^{-1}]	G [W m^{-3} K^{-1}]
#1	22 nm/ 12.5 μm	20 × /1.68 μm	4.1%	−0.249 ± 0.004	27.2	/
		50 × /0.58 μm	31.1%	−0.555 ± 0.008		8.13×10^{13}
		100 × /0.38 μm	37.6%	−0.704 ± 0.008		1.32×10^{14}
#2	26 nm/ 6.14 μm	20 × /1.63 μm	3.5%	−0.101 ± 0.002		/
		100 × /0.36 μm	22.5%	−0.394 ± 0.005		3.46×10^{14}

smaller thermal resistance case in supported 2D materials, this ratio becomes much larger. As reported in the work of Zobeiri et al. [33], the determined η is around 100%, 33%, and 11% for the E_{2g} mode under 100 × , 50 × , and 20 × objectives, respectively, for a supported 15.3 nm thick MoS_2 sample. This is because to reach the same AP temperature rise, a higher laser intensity is needed (since the total resistance is smaller) to heat up the sample. A higher laser intensity would generate a higher $\Delta\overline{T}_{OA}$. Therefore, the ratio $\eta = \Delta\overline{T}_{OA}/\Delta\overline{T}_{AP}$ is higher in supported 2D materials than suspended ones.

3. Thermal conductivity measurement of WS_2 based on real AP temperature

In this work, we will not use any laser absorption data or absolute temperature rise to determine the thermal conductivity. Rather, we will use our FET-Raman technique with full consideration of $\Delta\overline{T}_{OA}$ effect to do a high-profile measurement [32]. The FET-Raman method is developed from a frequency-resolved Raman method, in which the Raman excitation laser amplitude is modulated with a certain frequency and a duty cycle of 50%. Fig. 3a shows the physical scenario of the laser modulation and Raman response. During the laser-on period, the sample is heated to gradually approach a thermally steady state. It will reach the final thermally steady state when the laser-on period is long enough (longer than the thermal characteristic time of the sample). This situation will be identical to the CW laser heating in the steady state Raman method. Raman scattering mainly carries the steady state OP temperature because the initial transient state is short and can be neglected. When the modulating frequency increases, the sample cannot reach the thermally steady state during the laser-on period and the Raman scattering will carry the transient state OP temperature information. Moreover, in the laser-off period, the sample cannot cool down after one cycle of cooling, and the measured temperature rise response will have

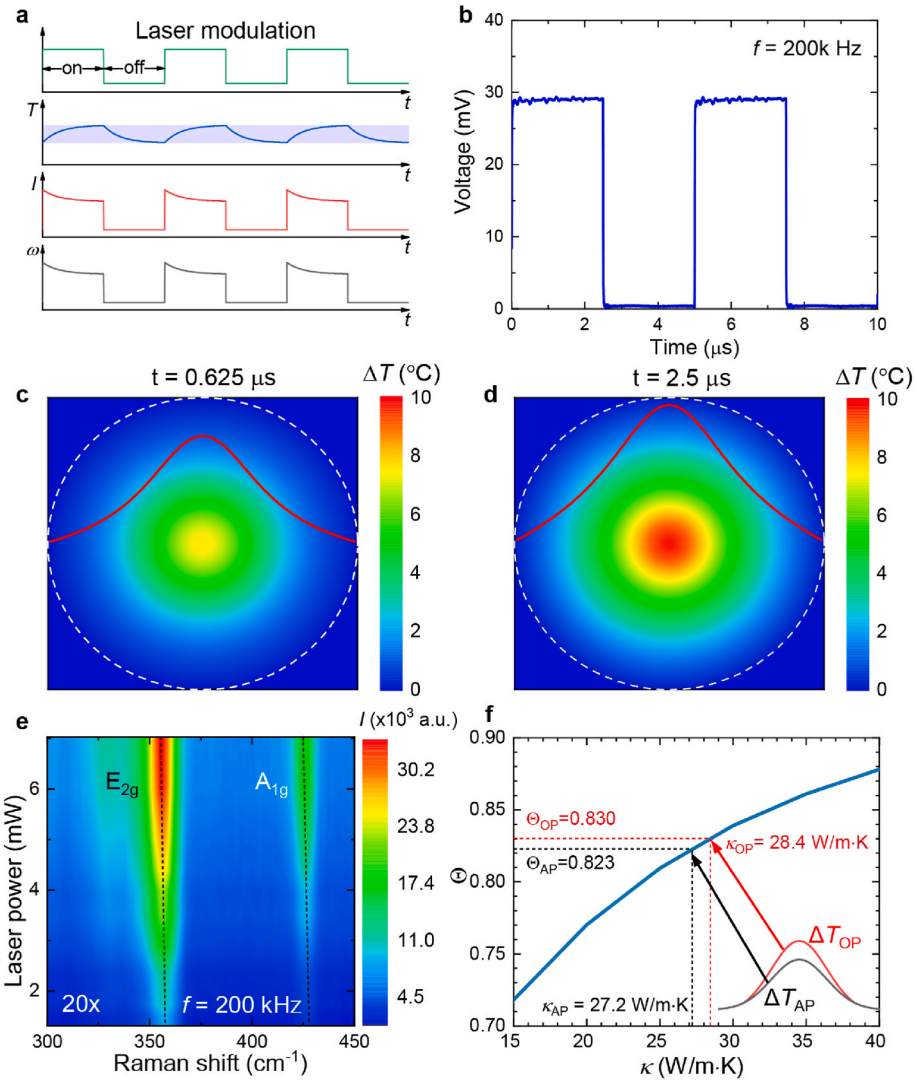

Fig. 3. Thermal conductivity measurement using FET-Raman. (a) Physics of the FET-Raman method. (b) Profile of the amplitude-modulated laser at 200 kHz frequency. (c), (d) Simulated temperature field in sample #1 over the hole at time of 0.625 μs (c) and 2.5 μs (d). The red curve depicts the temperature variation from the center of the hole to the edge. (e) Raman spectra against the laser power for sample #1 under the modulated laser with modulation frequency of 200 kHz. (f) Determination of the intrinsic thermal conductivity based on the temperature rise of APs. In comparison, κ determination based on temperature rise of OPs is also shown to demonstrate the error it will cause.

an accumulating effect from previous duty cycles. All these effects are considered in the FET-Raman physics modeling. It demonstrates that when the modulation frequency is extremely high, the sample will reach a quasi-steady state. The AP temperature rise at this state is half of the steady-state AP temperature rise, as only half the power is absorbed compared with that in the continuous heating case. Thus, two different energy transport states are established. It is noteworthy that both the FET-Raman and steady state Raman use the same laser source and optical delivery system, so $\Delta\overline{T}_{OA}$ is the same in these two cases. The above measured $\Delta\overline{T}_{OA}$ and also ψ_{OA} in the CW case from the last section can be directly used to subtract from the Raman measured ψ to obtain the real contribution of APs to the temperature rise and ψ in FET-Raman.

In the experimental investigation, a CW mode and a frequency-modulated mode of the laser are in turn used to heat the same suspended WS_2 film to the thermally steady state and transient state. Fig. 3b shows the high quality of the modulated laser used in the experiment. Under CW photon heating, the final AP temperature rise $\Delta T_{AP,cw}$ is mainly related to the absorption coefficient a and the intrinsic thermal conductivity κ of the WS_2 film. According to the governing equation in the above section, $\Delta T_{AP,cw}$ is proportional to a/κ. For FET-Raman measurement, the transient state energy transport process could be described by the following governing equation,

$$k\nabla^2 T_{AP,fr} + \dot{q} = \rho c_p \cdot \partial T_{AP,fr}/\partial t \tag{6}$$

where $T_{AP,fr}$ is the field of transient temperature rise in the film, $\dot{q}$ is the heat generation rate during the laser-on period, ρc_p the volumetric heat capacity of the WS_2 sample, and t is time. The final temperature rise for amplitude modulated heating can be expressed as the proportionality $T_{AP,fr} \propto a/(\rho c_p) f(\kappa/\rho c_p)$. The solved temperature fields in sample #1 at two selected moments in the transient heating process are shown in Fig. 3c and d. It clearly shows the development of the temperature field with time, and the rate of such development is determined by the thermophysical properties of the sample. Similar to the steady state Raman model, the Raman intensity weighted temperature $\overline{T}_{AP,fr}$ is needed for building a temperature rise ratio that cancels out the effect of the unknown parameters. Under amplitude modulated heating, this should be an average value not only over space but also over time,

$$\Delta\overline{T}_{AP,fr} = \int_0^t \int I \exp(-z/\tau_L) \Delta T_{AP,fr} dV dt \Big/ \int_0^t \int I \exp(-z/\tau_L) dV dt \tag{7}$$

where V_0 is the Raman scattering volume.

On the other hand, due to the fact that $\Delta\overline{T}_{AP,cw}$ and $\Delta\overline{T}_{AP,fr}$ in steady and transient energy transport states are the function of a, κ, and ρc_p, their ratio Θ_{AP} is proportional to $\kappa/[(\rho c_p) f(\kappa/\rho c_p)]$. Ignoring the change of ρc_p with temperature within the experimental temperature rise range (less than 50 °C), Θ_{AP} can be further simplified as only a function of κ. This treatment also avoids the influence of unknown parameters like a and χ_T.

In FET-Raman, the average AP temperature rise within the laser heating area under CW and amplitude-modulated case are used to construct a parameter as below:

$$\Theta_{AP} = \frac{\Delta\overline{T}_{AP,fr}}{\Delta\overline{T}_{AP,cw}} = \frac{\psi_{fr} - \eta\cdot\psi_{cw}}{(1-\eta)\psi_{cw}} = g(\kappa) \tag{8}$$

ψ is the experimental result from Raman measurement: $\psi_{cw} = -0.249 \pm 0.004\ cm^{-1}\ mW^{-1}$ (20 × objective) is the one measured under CW laser heating (Fig. 2f), and $\psi_{fr} = -0.207 \pm 0.003\ cm^{-1}\ mW^{-1}$ (20 × objective) is the one from FET-Raman (f = 200 kHz) (Fig. 3e). For sample #1, Θ_{AP} is 0.823 ± 0.018 measured under the 20 × objective.

Because an analytical relation between Θ_{AP} and κ is hard to obtain directly from Equation (8), we use high-fidelity computer modeling to build the relationship between Θ_{AP} and κ for sample #1 (Fig. 3f). In the modeling, since transient heat transfer is involved, the material's density ($\rho = 7500\ kg\ m^{-3}$) and specific heat ($c_p = 256.0\ J\ kg^{-1}\ K^{-1}$) of WS_2 [43] are also used. We use the constant density and specific heat at room temperature in the modeling since the temperature rise is low in the Raman experiment and has little effect on ρc_p. κ is determined by interpolating the theoretical curve to the measured Θ_{AP}. This determined κ is based on the AP temperature rise and represents the intrinsic κ of sample #1. Based on the evaluated Θ_{AP} of 0.823 ± 0.018, the intrinsic κ of sample #1 is determined to be $27.2^{+3.2}_{-2.9}\ W\ m^{-1}\ K^{-1}$. If the effect of $\Delta\overline{T}_{OA}$ is not subtracted, we would have Θ_{OP} = 0.830 ± 0.018, and the determined κ would be $28.4^{+4.2}_{-2.8}\ W\ m^{-1}\ K^{-1}$. The resulting error is about 4.4%. Though this error is small, one should notice this measurement has been conducted under the 20 × objective. This means that the laser spot radius at the focal plane is large; thus, $\Delta\overline{T}_{OA}$ ($\propto 1/r^2$) is not significant and will not raise much error when directly using the Raman determined. Also, the FET-Raman method employed above uses the ratio of ψ under CW and frequency-modulation scenarios. The effect of $\Delta\overline{T}_{OA}$ exists in both ψ_{cw} and ψ_{fr}. This will greatly reduce the effect of $\Delta\overline{T}_{OA}$ on Θ_{OP}. However, in most thermal measurements of two-dimensional materials using Raman methods, the 50 × and 100 × objectives are preferred in order to obtain a better Raman signal. $\Delta\overline{T}_{OA}$ is much greater under these two objectives. Taking the 100 × objective as an example, $\Delta\overline{T}_{OA}$ is about 37% of $\Delta\overline{T}_{AP}$ and will cause a large error of 37% if the normal steady-state Raman measurement is used. Therefore, it is clear an incomplete physical consideration of photon-induced thermal nonequilibrium will significantly undermine the accuracy of optothermal Raman methods. The determined κ of $27.2^{+3.2}_{-2.9}\ W\ m^{-1}\ K^{-1}$ agrees well with our previous measurement using the nanosecond ET-Raman technique: 22.8 and 23.8 $W\ m^{-1}\ K^{-1}$ for 49 and 60 nm thick free-standing WS_2 [44].

It is important to note that the resulting thermal conductivity is little larger than the literature value. This is because, in the referenced work, the Raman measured temperature was directly used to determine the thermal conductivity of WS_2 samples, and ΔT_{OA} was not excluded. The existence of ΔT_{OA} renders the measured Raman temperature (optical phonon temperature) to be higher than the real temperature (acoustic phonon temperature), which led to a smaller thermal conductivity. In the current work, we have eliminated the effect of ΔT_{OA}, and measured the intrinsic thermal conductivity of 2D WS_2. Another reason that may cause the difference in the measured thermal conductivity in referenced work and this work is the laser source. In the referenced work, both CW laser and ns laser were used, while only a CW laser is employed in the current work. The ns laser will generate more hot carriers and raise more thermal nonequilibrium. Under the ns laser irradiation, the hot carrier density will be very high which leads to a different thermal nonequilibrium state from that under the irradiation of CW laser. It will lower measurement accuracy. In the current work, we have used the frequency-modulated CW laser instead of the ns laser to ensure the same thermal nonequilibrium state in both CW and modulated (pulsed) energy transport states. This method will help lower the measurement uncertainty from the physical base of the method.

4. Energy coupling factor between OPs and APs

Under photon excitation, intense energy transfer happens from optical to acoustic phonons driven by their temperature difference ΔT_{OA}, as shown in Fig. 4a. Such a process is governed by the energy coupling factor G between them. At a specified location within the laser heating area, we have

$$\Delta T_{OA} \cdot G = I/\tau \tag{9}$$

where I is the intensity of the local optical field, and τ is optical absorption depth for WS_2 at the incident wavelength (532 nm). In our experiment I should consider the interference effect and $\Delta\overline{T}_{OA}$ is a Raman intensity weighted average temperature rise over the irradiated

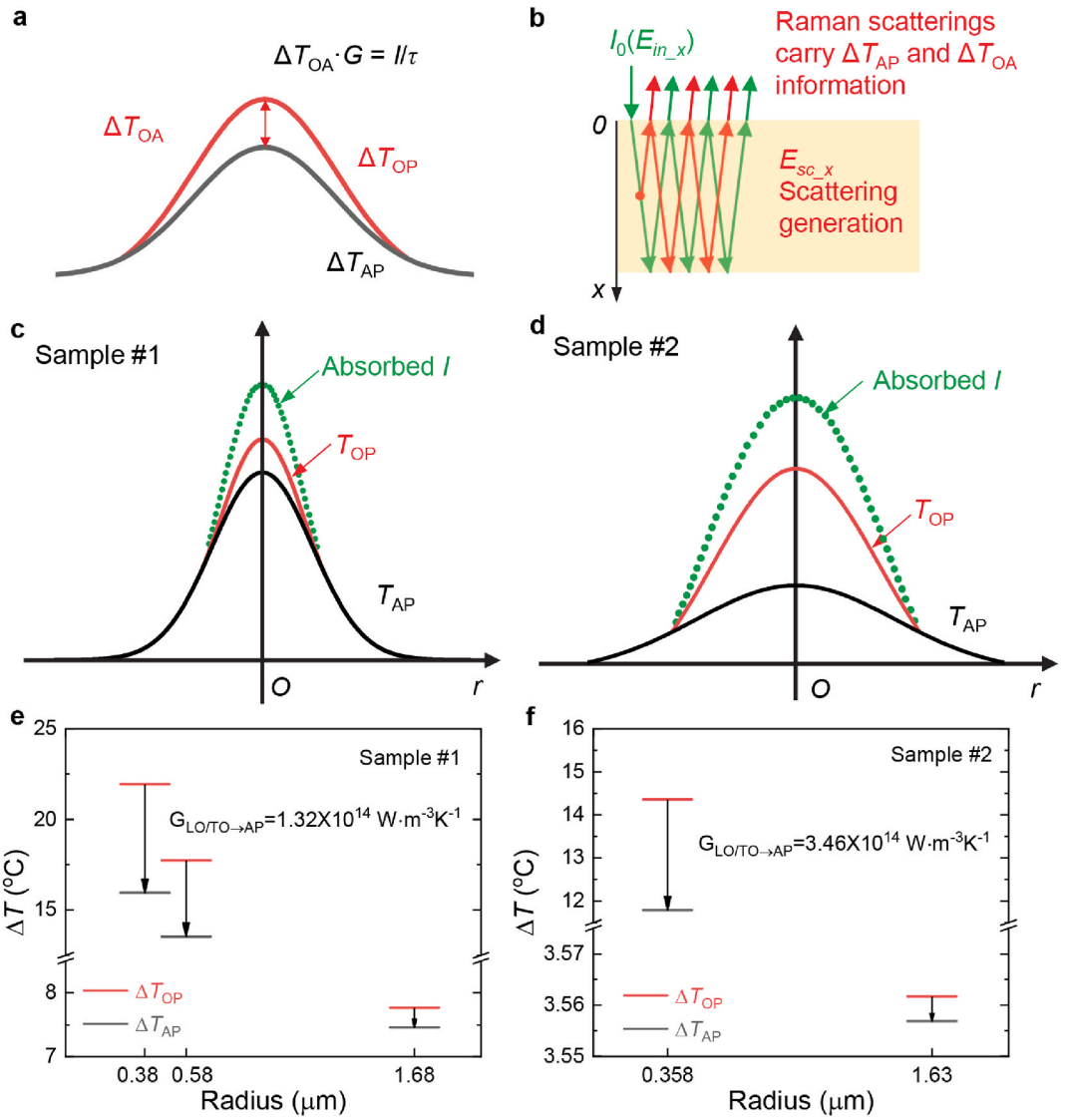

Fig. 4. Energy coupling between OPs and APs. (a) The schematics of the nonequilibrium between OPs and APs and the definition of the energy coupling factor. (b) The schematics for optical interference of incident laser and Raman scatterings in the film. (c), (d) The nonequilibrium temperature distribution in sample #1 (c) and sample #2 (d). (e), (f) Under a laser irradiation of 1 mW, the temperature rises of OPs and APs for sample #1 under 20 × , 50 × and 100 × objectives (e), and for sample #2 under 20 × and 100 × objective (f).

volume.

As shown in Fig. 4b, the incident laser beam is reflected at the top and bottom surfaces of the film repeatedly, and the intensity of the electric field located at x can be expressed as $E_{in\_x} = E_1^+ e^{i\beta_1 x} + E_1^- e^{-i\beta_1 x}$, where E_1^+ and E_1^- denote the forward and backward propagating electric fields at x, respectively; $\beta_1 = 2\pi\tilde{n}_1/\lambda$ where λ is the wavelength of the incident laser beam (532 nm); and $\tilde{n}_1 = 4.8845 + 0.9027i$ is the complex refractive index of WS_2 at 532 nm [42]. With full consideration of the local optical interference, the overall electric field at x becomes

$$E_{in\_x} = \frac{\tilde{t}_1 e^{-i\beta_1(L-x)} + \tilde{t}_1\tilde{r}_2 e^{i\beta_1(L-x)}}{e^{-i\beta_1 L} + \tilde{r}_1\tilde{r}_2 e^{i\beta_1 L}} E_0 \tag{10}$$

where $\tilde{t}_1 = 2n_0/(n_0+\tilde{n}_1)$, $\tilde{r}_1 = (n_0 - \tilde{n}_1)/(n_0+\tilde{n}_1)$, $\tilde{r}_2 = (\tilde{n}_1 - n_0)/(n_0+\tilde{n}_1)$, n_0 is the refractive index of air, and L is the thickness of the sample film. Integrating Equation (10) over the irradiated volume gives the real incident laser intensity absorbed by the WS_2 sample film: $I_{in} = \pi r_i^2 \cdot \frac{cn\varepsilon_0}{2} \int_{x=L} |E_{in\_x}|^2 \frac{2}{\tau} dx$ where ε_0 as 8.854×10^{-12} Fm^{-1} is the vacuum dielectric constant, r_i is the radius of the laser heating spot, and c as 3×10^8 m/s is the speed of light in vacuum.

Besides the incident optical field, the measured $\Delta\overline{T}_{OA}$ and $\Delta\overline{T}_{OP}$ is also affected by Raman scattering. The Raman scattering originates in the film and emits in all directions evenly, but only the components along the $\pm x$ direction will be reflected by the surfaces and finally received by the Raman spectrometer. Taking into account the interference effect on Raman emission, the electric field of the Raman scattering E_{sc_x} at x in the film has the expression [45].

$$E_{sc\_x} = \sqrt{\left|E_{sc\_x}^-\right|^2 + \left|E_{sc\_x}^+\right|^2} \tag{11}$$

where

$$E_{sc\_x}^- = \frac{\tilde{r}'_1}{\tilde{t}'_1} E_{sc,12}^+ e^{-i\beta'_1 L} + \frac{\tilde{r}'_2}{\tilde{t}'_1} E_{sc,12}^+ e^{i\beta'_1 L} + \frac{1}{\tilde{t}'_1} e^{i\beta'_1 x} \tag{12}$$

$$E_{sc\_x}^+ = \frac{\tilde{r}'_1}{\tilde{t}'_1} E_{sc,12}^+ e^{-i\beta'_1 L} - \frac{\tilde{r}'_1}{\tilde{t}'_1} e^{-i\beta'_1 x} + \frac{\tilde{r}'_2}{\tilde{t}'_1} E_{sc,12}^+ e^{i\beta'_1 L} \tag{13}$$

$$E^{+}_{sc,12}=\frac{-\tilde{r}_1 e^{i\beta'_1 x}}{e^{-i\beta'_1 L}+\tilde{r}_1\tilde{r}_2 e^{i\beta'_1 L}} \tag{14}$$

where $E^{+}_{sc\_x}$ and $E^{-}_{sc\_x}$ denote the forward and backward propagating electric fields for the generated Raman scattering from x. $\tilde{t}_1$, $\tilde{r}_1$, and $\tilde{r}_2$ are optical properties at the wavelength λ' of 542.2 nm corresponding to the E_{2g} mode: $\beta'_1 = 2\pi\tilde{n}_1/\lambda'$, $\tilde{t}_1 = 2n_0/(n_0+\tilde{n}_1)$, $\tilde{r}_1 = (n_0-\tilde{n}_1)/(n_0+\tilde{n}_1)$, and $\tilde{r}_2 = (\tilde{n}_1-n_0)/(n_0+\tilde{n}_1)$, in which $\tilde{n}_1 = 4.7472 + 0.7148i$ is the complex refractive index for the E_{2g} mode in the WS_2 layer [42].

Additionally, the Gaussian distribution of the incident laser beam and the Raman scattering interference further contribute to the spatial nonuniformity of the local ΔT_{OA}. Considering all the aforementioned effects, we have,

$$\Delta\overline{T}_{OA}=\frac{1}{2}\cdot\frac{\delta}{\tau G}\cdot\frac{cn_1\varepsilon_0}{2}\cdot\frac{\int_{x=L}|E_{in\_x}|^4\cdot|E_{sc\_x}|^2\mathrm{d}x}{\int_{x=L}|E_{in\_x}|^2\cdot|E_{sc\_x}|^2\mathrm{d}x} \tag{15}$$

where δ is the portion of laser energy transferred from the measured Raman mode OPs to APs. Assuming that the absorbed energy transferred from hot carriers to the three optical branches are uniform for order analysis, the E_{2g} mode is associated with both LO and TO branches and δ takes the value of 2/3. The A_{1g} mode is related to the ZO branch, and δ is equal to 1/3. In this work, to reduce the possible errors in data analysis, only the E_{2g} mode is taken into consideration as its Raman scattering is much stronger than that of the A_{1g} mode.

For sample #1, its κ is determined as $27.2^{+3.2}_{-2.9}$ $Wm^{-1}K^{-1}$. Using this κ in the simulation model together with a specified laser power (electric field E), a Raman intensity-weighted temperature rise can be calculated as $\Delta\overline{T}_{AP}$. Then $\Delta\overline{T}_{OA}$ is calculated as $\Delta\overline{T}_{OA} = \eta\Delta\overline{T}_{AP}$. Using Equation (15), the energy coupling factor can be determined with sound accuracy. For sample #1, the calculated Gs are 8.13×10^{13} and 1.32×10^{14} $Wm^{-3}K^{-1}$ from the 20 × /50 × and 20 × /100 × cases, respectively, and 3.46×10^{14} $Wm^{-3}K^{-1}$ for sample #2 (Table 2 and Fig. 4e and f). The same order of magnitude was observed for the coupling factor between optical phonons and acoustic phonons for the LO and TO branches in MoS_2 and $MoSe_2$, 2.26×10^{14} and 4.9×10^{14} $W\,m^{-3}\,K^{-1}$, in Wang's work [38]. For sample #1, the two determined energy coupling factors are close, substantiating that the G is less affected by the laser spot size. The higher uncertainty in the 20 × /50 × case compared to the 20 × /100 × case may contribute to the difference between these two results. Thus, the determined G of 1.32×10^{14} $Wm^{-3}K^{-1}$ from the 20 × /100 × case is more reliable for sample #1. Sample #2 has a smaller diameter hole meaning it has a smaller thermal resistance. To reach a similar level in ψ, higher energy input is needed for sample #2 (Fig. 4d) than sample #1 (Fig. 4c). The measured higher G for Sample #2 can be explained by the higher concentration of hot carriers excited by the photon flux, which will induce more phonon scatterings (smaller phonon life time τ_p) [36], leading to higher energy coupling factor (proportional to τ_p^{-1} between phonon branches). A similar observation was also made in the work by Wang et al. [38].

The technique developed in this work can be extended to any suspended 2D materials of arbitrary geometry. To be specific, under one laser spot with a geometry factor of Ω_1, its AP temperature rise can be written as $\Delta T_1 = E/\kappa\cdot f(\Omega_1,\Omega_h)$. E is the total absorbed laser power, Ω_h is the geometry factor of the suspending hole, and $f(\Omega_1,\Omega_h)/\kappa$ represents the thermal resistance of the sample. When changing to another laser spot of Ω_2 geometry factor, the AP temperature rise will be $\Delta T_2 = E/\kappa\cdot f(\Omega_2,\Omega_h)$. The ratio $\Delta T_1/\Delta T_2 = f(\Omega_1,\Omega_h)/f(\Omega_2,\Omega_h)$ is only a function of geometry factors, and it is a well-defined invariant for a specific sample under known experimental conditions. Even for irregular laser spots or hole structures, numerical simulations can give the exact value of this invariant. Further combined with the Raman measured ψ ratio, we can readily determine the effect of ΔT_{OA} and measure the intrinsic κ. More importantly, the above method extension largely weakens the limitations imposed by sample preparation (sample geometry control) and irradiation condition. Also, the optical absorption coefficient and Raman temperature coefficient of the 2D material are not needed in FET-Raman. This provides great advantages for studying and designing new 2D materials.

5. Conclusions

In summary, an AP thermal field invariant has been designed: $\xi_{AP} = \Delta\overline{T}_{AP,1}/\Delta\overline{T}_{AP,2}$ to distinguish the OP and AP temperatures. Raman-measured ξ_{OP} deviated from ξ_{AP} and was used successfully to distinguish $\Delta\overline{T}_{OA}$ from $\Delta\overline{T}_{OP}$. The percentage of $\Delta\overline{T}_{OA}$ to $\Delta\overline{T}_{AP}$ was measured to be 4.1% and 37.6% under the 20 × and 100 × objectives for a suspended 22 nm-thin WS_2 of 12.5 μm diameter. Using $\Delta\overline{T}_{AP}$, the real κ of WS_2 was measured to be $27.2^{+3.2}_{-2.9}$ $Wm^{-1}K^{-1}$ using our FET-Raman technique. ET-Raman does not need information on photon absorption or absolute temperature rise, and carries minimal error. The energy coupling factor between LO/TO OPs and APs was determined to be around 10^{14} W $m^{-3}K^{-1}$ based on fully considered optical interference and intrinsic κ. The methodology developed in this work can be generalized to any suspended 2D materials of arbitrary geometry. This significantly advances the physics characterization and design of thermophysical properties of 2D materials.

Funding

Partial support of this work by National Science Foundation (CBET1930866 and CMMI2032464 for. X.W.), National Key Research and Development Program (No.2019YFE0119900 for H. L.), National Natural Science Foundation of China (No. 52106220 for S. X.), and China Scholarship Council (No. 201908310026 for S. X.) is gratefully acknowledged.

Declaration of competing interest

The authors declare that they have no known competing financial interests or personal relationships that could have appeared to influence the work reported in this paper.

Data availability

Data will be made available on request.

References

[1] S. Manzeli, D. Ovchinnikov, D. Pasquier, O.V. Yazyev, A. Kis, 2D transition metal dichalcogenides, Nat. Rev. Mater. 2 (2017): 17033, https://doi.org/10.1038/natrevmats.2017.33.
[2] J. Zhang, B. Tan, X. Zhang, F. Gao, Y. Hu, L. Wang, X. Duan, Z. Yang, P. Hu, Atomically thin hexagonal boron nitride and its heterostructures, Adv. Mater. 33 (2021): 2000769, https://doi.org/10.1002/adma.202000769.
[3] Y. Du, W. Zhou, J. Gao, X. Pan, Y. Li, Fundament and application of graphdiyne in electrochemical energy, Accounts Chem. Res. 53 (2020) 459–469, https://doi.org/10.1021/acs.accounts.9b00558.
[4] L. Pi, L. Li, K. Liu, Q. Zhang, H. Li, T. Zhai, Recent progress on 2D noble-transition-metal dichalcogenides, Adv. Funct. Mater. 29 (2019): 1904932, https://doi.org/10.1002/adfm.201904932.
[5] A.J. Mannix, Z. Zhang, N.P. Guisinger, B.I. Yakobson, M.C. Hersam, Borophene as a prototype for synthetic 2D materials development, Nat. Nanotechnol. 13 (2018) 444–450, https://doi.org/10.1038/s41565-018-0157-4.
[6] X. Yang, X. Li, Y. Deng, Y. Wang, G. Liu, C. Wei, H. Li, Z. Wu, Q. Zheng, Z. Chen, Q. Jiang, H. Lu, J. Zhu, Ethanol assisted transfer for clean assembly of 2D building blocks and suspended structures, Adv. Funct. Mater. 29 (2019): 1902427, https://doi.org/10.1002/adfm.201902427.
[7] B. Radisavljevic, A. Radenovic, J. Brivio, V. Giacometti, A. Kis, Single-layer MoS_2 transistors, Nat. Nanotechnol. 6 (2011) 147–150, https://doi.org/10.1038/nnano.2010.279.

[8] L. Li, Y. Yu, G.J. Ye, Q. Ge, X. Ou, H. Wu, D. Feng, X.H. Chen, Y. Zhang, Black phosphorus field-effect transistors, Nat. Nanotechnol. 9 (2014) 372–377, https://doi.org/10.1038/nnano.2014.35.
[9] M. Bernardi, M. Palummo, J.C. Grossman, Extraordinary sunlight absorption and one nanometer thick photovoltaics using two-dimensional monolayer materials, Nano Lett. 13 (2013) 3664–3670, https://doi.org/10.1021/nl401544y.
[10] O. Lopez-Sanchez, D. Lembke, M. Kayci, A. Radenovic, A. Kis, Ultrasensitive photodetectors based on monolayer MoS_2, Nat. Nanotechnol. 8 (2013) 497–501, https://doi.org/10.1038/nnano.2013.100.
[11] S. Zhang, H. Luo, S. Wang, Z. Chen, S. Nie, C. Liu, J. Song, A thermal actuated switchable dry adhesive with high reversibility for transfer printing, Int. J. Extrem. Manuf. 3 (2021): 035103, https://doi.org/10.1088/2631-7990/abff69.
[12] W. Wu, L. Wang, Y. Li, F. Zhang, L. Lin, S. Niu, D. Chenet, X. Zhang, Y. Hao, T. F. Heinz, J. Hone, Z.L. Wang, Piezoelectricity of single-atomic-layer MoS_2 for energy conversion and piezotronics, Nature 514 (2014) 470–474, https://doi.org/10.1038/nature13792.
[13] D. Tan, M. Willatzen, Z.L. Wang, Electron transfer in the contact-electrification between corrugated 2D materials: A first-principles study, Nano Energy 79 (2021): 105386, https://doi.org/10.1016/j.nanoen.2020.105386.
[14] T. Terada, Y. Uematsu, T. Ishibe, N. Naruse, K. Sato, T.Q. Nguyen, E. Kobayashi, H. Nakano, Y. Nakamura, Giant enhancement of Seebeck coefficient by deformation of silicene buckled structure in calcium-intercalated layered silicene, Film 9 (2022): 2101752, https://doi.org/10.1002/admi.202101752.
[15] Z. Chang, K. Liu, Z. Sun, K. Yuan, S. Cheng, Y. Gao, X. Zhang, C. Shen, H. Zhang, N. Wang, D. Tang, First-principles investigation of the significant anisotropy and ultrahigh thermoelectric efficiency of a novel two-dimensional $Ga_2I_2S_2$ at room temperature. https://doi.org/10.1088/2631-7990/ac5f0f, 2022, 4.
[16] J. Deng, D. Deng, X. Bao, Robust catalysis on 2D materials encapsulating metals: concept, Appl. Perspect. 29 (2017): 1606967, https://doi.org/10.1002/adma.201606967.
[17] D. Deng, K.S. Novoselov, Q. Fu, N. Zheng, Z. Tian, X. Bao, Catalysis with two-dimensional materials and their heterostructures, Nat. Nanotechnol. 11 (2016) 218–230, https://doi.org/10.1038/nnano.2015.340.
[18] S. Xu, A. Fan, H. Wang, X. Zhang, X. Wang, Raman-Based nanoscale thermal transport characterization: a critical review, Int. J. Heat Mass Tran. 154 (2020): 119751, https://doi.org/10.1016/j.ijheatmasstransfer.2020.119751.
[19] Y. Yue, J. Zhang, Y. Xie, W. Chen, X. Wang, Energy coupling across low-dimensional contact interfaces at the atomic scale, Int. J. Heat Mass Tran. 110 (2017) 827–844, https://doi.org/10.1016/j.ijheatmasstransfer.2017.03.082.
[20] R. Wang, S. Xu, Y. Yue, X. Wang, Thermal behavior of materials in laser-assisted extreme manufacturing: Raman-based novel characterization, Int. J. Extrem. Manuf. 2 (2020): 032004, https://doi.org/10.1088/2631-7990/aba17c.
[21] A.A. Balandin, S. Ghosh, W. Bao, I. Calizo, D. Teweldebrhan, F. Miao, C.N. Lau, Superior thermal conductivity of single-layer graphene, Nano Lett. 8 (2008) 902–907, https://doi.org/10.1021/nl0731872.
[22] Y. Yue, X. Chen, X. Wang, Noncontact sub-10 nm temperature measurement in near-field laser heating, ACS Nano 5 (2011) 4466–4475, https://doi.org/10.1021/nn2011442.
[23] Y. Yue, J. Zhang, X. Wang, Micro/nanoscale spatial resolution temperature probing for the interfacial thermal characterization of epitaxial graphene on 4H-SiC, Small 7 (2011) 3324–3333, https://doi.org/10.1002/smll.201101598.
[24] X. Tang, S. Xu, J. Zhang, X. Wang, Five orders of magnitude reduction in energy coupling across corrugated graphene/substrate interfaces, ACS Appl. Mater. Interfaces 6 (2014) 2809–2818, https://doi.org/10.1021/am405388a.
[25] X. Tang, S. Xu, X. Wang, Corrugated epitaxial graphene/SiC interfaces: photon excitation and probing, Nanoscale 6 (2014) 8822–8830, https://doi.org/10.1039/c4nr00410h.
[26] S. Xu, T. Wang, D.H. Hurley, Y. Yue, X. Wang, Development of time-domain differential Raman for transient thermal probing of materials, Opt Express 23 (2015) 10040–10056, https://doi.org/10.1364/OE.23.010040.
[27] T. Wang, S. Xu, D.H. Hurley, Y. Yue, X. Wang, Frequency-resolved Raman for transient thermal probing and thermal diffusivity measurement, Opt. Lett. 41 (2016) 80–83, https://doi.org/10.1364/OL.41.000080.
[28] T. Wang, M. Han, R. Wang, P. Yuan, S. Xu, X. Wang, Characterization of anisotropic thermal conductivity of suspended nm-thick black phosphorus with frequency-resolved Raman spectroscopy, J. Appl. Phys. 123 (2018): 145104, https://doi.org/10.1063/1.5023800.
[29] P. Yuan, H. Tan, R. Wang, T. Wang, X. Wang, Very fast hot carrier diffusion in unconstrained MoS_2 on a glass substrate: discovered by picosecond ET-Raman, RSC Adv. 8 (2018) 12767–12778, https://doi.org/10.1039/c8ra01106k.
[30] P. Yuan, R. Wang, H. Tan, T. Wang, X. Wang, Energy transport state resolved Raman for probing interface energy transport and hot carrier diffusion in few-layered MoS_2, ACS Photonics 4 (2017) 3115–3129, https://doi.org/10.1021/acsphotonics.7b00815.
[31] N. Hunter, N. Azam, H. Zobeiri, R. Wang, M. Mahjouri-Samani, X. Wang, Interfacial thermal conductance between monolayer WSe_2 and SiO_2 under consideration of radiative electron-hole recombination, ACS Appl. Mater. Interfaces 12 (2020) 51069–51081, https://doi.org/10.1021/acsami.0c14990.
[32] H. Zobeiri, R. Wang, T. Wang, H. Lin, C. Deng, X. Wang, Frequency-domain energy transport state-resolved Raman for measuring the thermal conductivity of suspended nm-thick MoSe2, Int. J. Heat Mass Tran. 133 (2019) 1074–1085, https://doi.org/10.1016/j.ijheatmasstransfer.2019.01.012.
[33] H. Zobeiri, N. Hunter, N. Van Velson, C. Deng, Q. Zhang, X. Wang, Interfacial thermal resistance between nm-thick MoS_2 and quartz substrate: a critical revisit under phonon mode-wide thermal non-equilibrium, Nano Energy 89 (2021): 106364, https://doi.org/10.1016/j.nanoen.2021.106364.
[34] R. Wang, N. Hunter, H. Zobeiri, S. Xu, X. Wang, Critical problems faced in Raman-based energy transport characterization of nanomaterials, Phys. Chem. Chem. Phys. (2022), https://doi.org/10.1039/D2CP02126A. In press.
[35] A.K. Vallabhaneni, D. Singh, H. Bao, J. Murthy, X. Ruan, Reliability of Raman measurements of thermal conductivity of single-layer graphene due to selective electron-phonon coupling: a first-principles study, Phys. Rev. B 93 (2016): 125432, https://doi.org/10.1103/PhysRevB.93.125432.
[36] Z. Lu, A. Vallabhaneni, B. Cao, X. Ruan, Phonon branch-resolved electron-phonon coupling and the multitemperature model, Phys. Rev. B 98 (2018): 134309, https://doi.org/10.1103/PhysRevB.98.134309.
[37] S. Sullivan, A. Vallabhaneni, I. Kholmanov, X. Ruan, J. Murthy, L. Shi, Optical generation and detection of local nonequilibrium phonons in suspended graphene, Nano Lett. 17 (2017) 2049–2056, https://doi.org/10.1021/acs.nanolett.7b00110.
[38] R. Wang, H. Zobeiri, Y. Xie, X. Wang, X. Zhang, Y. Yue, Distinguishing optical and acoustic phonon temperatures and their energy coupling factor under photon excitation in nm 2D materials, Adv. Sci. 7 (2020): 2000097, https://doi.org/10.1002/advs.202000097.
[39] H. Zobeiri, N. Hunter, R. Wang, T. Wang, X. Wang, Direct characterization of thermal nonequilibrium between optical and acoustic phonons in graphene paper under photon excitation, Adv. Sci. 8 (2021): 2004712, https://doi.org/10.1002/advs.202004712.
[40] R. Wang, T. Wang, H. Zobeiri, P. Yuan, C. Deng, Y. Yue, S. Xu, X. Wang, Measurement of the thermal conductivities of suspended MoS_2 and $MoSe_2$ by nanosecond ET-Raman without temperature calibration and laser absorption evaluation, Nanoscale 10 (2018) 23087–23102, https://doi.org/10.1039/c8nr05641b.
[41] F. Zhang, Y. Lu, S. Schulman Daniel, T. Zhang, K. Fujisawa, Z. Lin, Y. Lei, L. Elias Ana, S. Das, B. Sinnott Susan, M. Terrones, Carbon doping of WS_2 monolayers: bandgap reduction and p-type doping transport, Sci. Adv. 5 (2019): eaav5003, https://doi.org/10.1126/sciadv.aav5003.
[42] H.-L. Liu, C.-C. Shen, S.-H. Su, C.-L. Hsu, M.-Y. Li, L.-J. Li, Optical properties of monolayer transition metal dichalcogenides probed by spectroscopic ellipsometry, Appl. Phys. Lett. 105 (2014): 201905, https://doi.org/10.1063/1.4901836.
[43] B. Peng, H. Zhang, H. Shao, Y. Xu, X. Zhang, H. Zhu, Thermal conductivity of monolayer MoS_2, $MoSe_2$, and WS_2: interplay of mass effect, interatomic bonding and anharmonicity, RSC Adv. 6 (2016) 5767–5773, https://doi.org/10.1039/c5ra19747c.
[44] H. Zobeiri, R. Wang, Q. Zhang, G. Zhu, X. Wang, Hot carrier transfer and phonon transport in suspended nm WS_2 films, Acta Mater. 175 (2019) 222–237, https://doi.org/10.1016/j.actamat.2019.06.011.
[45] N.V. Velson, H. Zobeiri, X. Wang, Rigorous prediction of Raman intensity from multi-layer films, Opt Express 28 (2020) 35272–35283, https://doi.org/10.1364/OE.403705.